J. Fluid Mech. (2000), *vol.* 410, *pp.* 343–366. Printed in the United Kingdom

Turbulent kinetic energy transport in a corner formed by a solid wall and a free surface

By T. Y. HSU[1], L. M. GREGA[2], R. I. LEIGHTON[3] AND T. WEI[1]

[1]Department of Mechanical and Aerospace Engineering, Rutgers; The State University of New Jersey Piscataway, NJ 08854-8058, USA
[2]Structural Acoustics and Hydroacoustics Branch, Naval Surface Warfare Center West Bethesda, MD 20817-5700, USA
[3]Remote Sensing Division, Naval Research Laboratory, Washington, DC 20375, USA

(Received 29 June 1998 and in revised form 13 December 1999)

High-resolution DPIV and LDV measurements were made in a turbulent mixed-boundary corner, i.e. a turbulent boundary layer generated by horizontal flow of water along a vertical wall in the vicinity of a horizontal free surface. This work is an extension of an earlier numerical/experimental study which established the existence of inner and outer secondary flow regions in the corner. The inner secondary motion is characterized by a weak, slowly evolving vortex with negative streamwise vorticity. The outer secondary motion is characterized by an upflow along the wall and outflow away from the wall at the free surface. The objective of the current investigation, then, was to understand the combined effects of a horizontal, shear-free, free surface and a vertical, rigid, no-slip boundary on turbulent kinetic energy transport. The context of this work is providing physical insights and quantitative data for advancing the state of the art in free-surface turbulence modelling. Experiments were conducted in a large free-surface water tunnel at momentum-thickness Reynolds numbers, Re_θ, of 670 for the DPIV studies, and 1150 for the LDV measurements. A high-resolution, two-correlation DPIV program was used to generate ensembles of vector fields in planes parallel to the free surface. These data were further processed to obtain profiles of turbulent kinetic energy transport terms, such as production and dissipation. In addition, profiles of streamwise and surface-normal velocity were made (as functions of distance from the wall) using two-component LDV. Key findings of this study include the fact that both turbulent kinetic energy production and dissipation are dramatically reduced close to the free surface. Far from the wall, this results in an increase in surface-parallel fluctuations very close to the free surface. The degree of this anisotropy and the spatial scales over which it exists are critical data for improved free-surface turbulence models.

1. Introduction

1.1. *Background*

Over the past decade, the effect of free surfaces on turbulent liquid flows has received a great deal of attention. This is particularly important in problems such as modelling the air–sea interface, remote sensing, sediment transport in rivers, and manufacturing processes such as paper-making.

A common finding of all of these studies is the existence of a free-surface current which causes lateral spreading of near-surface turbulence. This seems to occur regardless of the type of flow – jets, wakes, or boundary layers. Examples of different geometries exhibiting surface currents include the jet studies of Anthony & Willmarth (1992), wake measurements by Logory, Hirsa & Anthony (1996), and the preceding mixed-boundary corner study of Grega *et al.* (1995).

The existence of free-surface currents is but one indication that turbulence close to a liquid–gas interface is highly anisotropic. As such, standard turbulence models would incorrectly predict flow close to a free surface. The need for accurate turbulence models is highlighted in the work of Thomas & Williams (1995). In that study, the authors used large-eddy simulation (LES) techniques to examine turbulence in an asymmetric compound open channel. Many of the features reported in Grega *et al.* (1995) are also persent in Thomas & Williams' results. However, Thomas & Williams' (1995) study lacks detail in the near-corner region; this is presumably due to the need for both higher grid resolution and for better anisotropic turbulence models. From a modelling prespective, therefore, it is important to know the degree of anisotropy as well as the length scales over which the free-surface anisotropic effects are present. To this end, a number of studies have been conducted of isotropic turbulence in the vicinity of a free surface.

The starting point for much of the recent isotropic turbulence–free-surface interaction research was a body of work including Uzkan & Reynolds (1967), Thomas & Hancock (1977), and Hunt & Graham (1978). These studies, the first two were experimental and the last was theoretical, addressed the problem of isotropic grid turbulence in the vicinity of a rigid boundary moving at the mean flow speed. While the principal focus of these works was on understanding the dynamic importance of large, outer-region motions in turbulent boundary layers, they provide significant insights into the effect of a free surface on turbulent transport.

A key finding from these earlier studies, particularly from the theoretical analysis of Hunt & Graham (1978), was the existence of two length scales. While their analysis was strictly valid for short times only (the insertion problem), it has provided insights into the concepts of a near-boundary viscous length and a larger source layer. These concepts were examined numerically by Perot & Moin (1995) and Walker, Leighton & Garza-Rios (1996). The former examined the insertion of a variety of boundaries into isotropic turbulence, while the latter considered only the effects of a rigid shear-free boundary on isotropic turbulence.

As part of their analysis, Walker *et al.* (1996) computed terms of the turbulent kinetic energy transport equation. An important finding from this calculation was that the isotropic dissipation function is reduced near the free surface. The reduction is primarily due to the stress-free boundary condition. A result of reduced dissipation is the apparent increase of turbulence kinetic energy at the interface. Near the interface, they found that anisotropic dissipation is largely responsible for velocity fluctuations becoming anisotropic, a fact that, of course, directly addresses the importance of accurate modelling of the free surface.

In spite of its importance to turbulence modelling, turbulent kinetic energy transport in the mixed-boundary corner formed by a horizontal free surface and a vertical wall has received little attention to date. Accurate models are particularly necessary for this problem because turbulent flow along a mixed-boundary corner has engineering relevance in a variety of problems ranging from sediment transport in river channels to pulp fibre control in paper-making. In the latter example, the paper industry depends heavily on turbulent strain fields in the paper sheet-forming region to control the

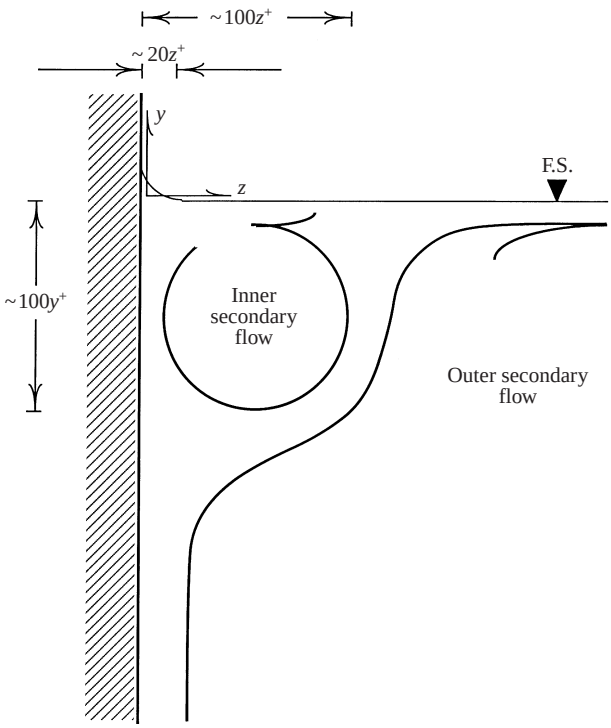

FIGURE 1. Simplified schematic drawing of the inner and outer secondary flow model proposed by Grega *et al.* (1995). The bulk flow direction is out of the page.

quality of the final product. For recent measurements on the topic, the reader is referred to Shah *et al.* (1999). Material waste resulting from interactions with side fences is a critical problem in this multi-billion dollar industry.

The turbulent mixed-boundary corner was first examined in detail by Grega *et al.* (1995), and more recently by Longo, Huang & Stern (1998) and Sreedhar & Stern (1998). Grega *et al.* (1995) examined the mixed-boundary corner formed along the sidewall of a water tunnel close to the free surface. In contrast, Longo *et al.* (1998) examined the flow adjacent to a surface-piercing plate towed through a quiescent tank. Sreedhar & Stern (1998) examined differences in horizontal boundary conditions using a compressible, temporally evolving LES calculation. While there are similarities between the studies, there are also significant differences which inhibit direct comparison and which highlight the need for additional work.

A unifying theme in all of these works is the existence of mean secondary flows in the near-corner region, phenomena also discernible in the work of Thomas & Williams (1995). As best as can be determined, secondary flows consist of an inner secondary vortex, and an outer secondary flow as shown in the cross-stream schematic drawing in figure 1. The inner secondary vortex is clearly resolved in the computational results shown in Grega *et al.* (1995), and to a lesser degree in Sreedhar & Stern (1998). The spatial measurement resolution in Longo *et al.* (1998) was insufficient to resolve the inner secondary vortex motion. The single-component velocity measurements in Grega *et al.* (1995) did not permit visualization of this flow at all.

The inner secondary vortex is a weak vortex with flow in toward the wall at the free surface and down away from the free surface along the wall. This is analogous

to the secondary vortices found in flow along a corner formed by two solid walls. Like the solid–solid corner, circumferential velocities in the solid–free-surface corner vortex are on the order of 1% of the mean stream speed. As such, the inner secondary vortex is essentially a mean phenomenon; one would not expect to see such a vortex in an instantaneous cross-stream measurement. The origin of the inner secondary flow in the context of vorticity transport is the topic of a follow-on study currently in progress.

The outer secondary flow, also shown in figure 1, is the mean surface current responsible for the transverse spreading of turbulence at the free surface. In this flow, turbulent boundary layer fluid is transported up toward the free surface along the wall, around the inner secondary vortex and out away from the wall at the free surface. This free-surface current results in the thickening of the vertical-wall turbulent boundary layer at the free surface reported by Grega *et al.* (1995).

While the existence of secondary flows is common to the works of Grega *et al.* (1995), Longo *et al.* (1998), and Sreedhar & Stern (1998), it was previously noted that there are fundamental differences between the studies as well. In particular, where the turbulence examined in Grega *et al.* (1998) was temporally stationary, it is not clear that flow in Longo *et al.* (1998) had reached a similar state. On another hand, the work of Sreedhar & Stern (1998) was a compressible LES calculation using a temporally evolving code. It is the differences between these studies which highlight the need for careful measurements in a clearly defined flow. Of particular interest in this paper is the transport of turbulent kinetic energy. To see the differences, it will be useful to contrast the three different studies in the following paragraphs.

The starting point for the current work is the earlier investigation of Grega *et al.* (1995). In that study, measurements were made on the sidewall of a closed-loop water tunnel with sampling times in excess of thirty minutes. Since the tunnel could be (and was) left running for as long as necessary, there was no question that the formation of the secondary flow patterns was complete and the flow was temporally stationary. The key limitation of those experiments, in the context of the present work, was that only single-point velocity measurements were made, thereby limiting the scope of the investigation.

A comparison between the streamwise turbulence intensity profiles in Grega *et al.* (1995) and the present study is shown in figure 2. Both of these wall-normal profiles were made using laser Doppler velocimetry (LDV) systems approximately 60 viscous lengths below the free surface. The data from Grega *et al.* (1995) were obtained using a single-component LDV system while the present data were obtained with a three-component system. To within the accuracy of determining friction velocity and wall location, the agreement between the two profiles is reasonably good. One would hope that this were the case given that the flow facilities are identical.

For completeness, it should be noted here that there were internal inconsistencies between the experiments and the DNS data reported in Grega *et al.* (1995). These were chiefly due to the fact that the computational domain was 300 viscous units wide while the experimental facility was over 4000 viscous units wide. The effect of symmetry at the centreline was prominent in the computations, but not an issue in the experiments. This matter will be reintroduced later in this paper in the presentation and discussion of results.

The experiments of Longo *et al.* (1998) consisted of three-component LDV measurements made near a 1.2 m long, surface-piercing plate being towed in a 100 m long tank. Measurements were initiated shortly after the tow carriage had reached constant speed, and the maximum possible sampling time reported was 75 s. Given

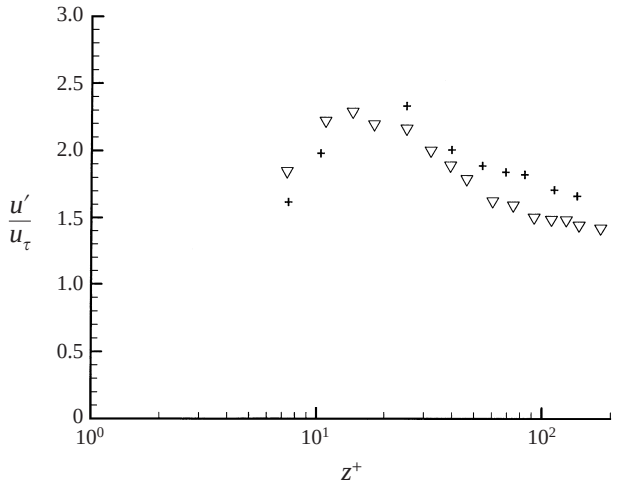

FIGURE 2. Comparison of u'/u_τ vs. z^+ profiles between data from +, Grega *et al.* (1995) and ▽, the present study. Both profiles were obtained using LDV at a distance of ~ 60 viscous lengths below the free surface.

that the eddy turnover time of the inner secondary vortex was on the order of tens of seconds, it is not at all clear that the secondary flows in the tow tank experiments had sufficient time to reach steady state. Thus where Grega *et al.* (1995) reported on the steady-state secondary flow, it appears that Longo *et al.* (1998) examined the temporally evolving case. Unfortunately comparisons between these two papers is problematic owing to difficulties in establishing common non-dimensionalizations. Comparisons to Sreedhar & Stern (1998) however were possible.

The computational work of Sreedhar & Stern (1998) contrasted differences between a corner formed by two solid walls and the mixed-boundary corner. The free surface in the mixed-boundary flow was modelled as a rigid, shear-free boundary. A temporally evolving, compressible code was used in which the initial condition was a turbulent boundary layer solution. The Mach number for these calculations was 0.4. Although the authors contended that the flow was essentially incompressible, it seems unlikely that compressibility effects were truly absent.

A separate issue in Sreedhar & Stern (1998) was the convergence of the data. For the solid–solid corner calculations, one would expect to see a line of symmetry along the angle bisector between the two walls. Detailed measurements by Gessner & Jones (1961, 1965) clearly show this. One would also expect to see smooth contours if sufficient averaging had been done. Neither was the case, however, in Sreedhar & Stern (1998). There was no symmetry along the 45° corner bisector, and even the mean contours exhibit a fair amount of waviness. Unfortunately, this raises questions regarding the accuracy of the calculations.

Figure 3 contains comparisons between present measurements and LES results by Sreedhar & Stern (1998) for free-surface-normal profiles of streamwise fluctuations and free-surface-normal velocity fluctuations. Again data from the three-component LDV measurements described later in this paper are included. The plot shows u'/U and v'/U as functions of distance below the free surface at a distance of ~ 60 viscous lengths from the vertical solid wall. Note that y^+ denotes the free-surface-normal direction, or the direction opposite that in which gravity acts. In order to make this

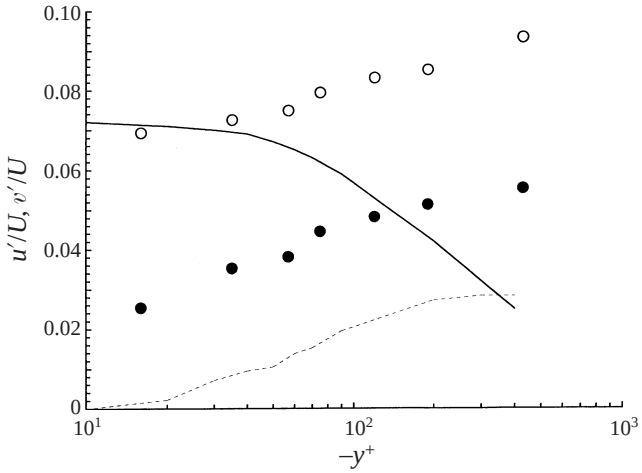

FIGURE 3. Comparison of turbulence intensity profiles as a function of distance below the free surface. ———, u'/U LES results of Sreedhar & Stern (1998); – – – –, v'/U LES results of Sreedhar & Stern (1998); ○, u'/U present (LDV); ●, v'/U present (LDV).

comparison, estimates of the dimension of a viscous length for the LES data had to be made based on the descriptions provided by Sreedhar & Stern (1998).

Clearly there is little agreement between the experiments and the LES results. In the LES studies, streamwise fluctuations are predicted to decrease, where they increase in the experiments. The LES also appears to grossly underpredict the magnitude of the free-surface-normal fluctuations throughout the flow. The present authors have also computed the anisotropy tensor profiles shown in both Longo *et al.* (1998) and Sreedhar & Stern (1998) and found similarly dramatic discrepancies. This is, of course, not surprising given that the more fundamental quantities, i.e. mean-square velocity fluctuations, do not even agree.

Setting aside the compressibility and convergence issues, a critical feature of the computational methodology used by Sreedhar & Stern (1998) in the context of the current work, was the use of a compressible Smagorinsky subgrid-scale model. Such models inherently assume isotropy of small-scale turbulence, an assumption which does not appear to be valid for the mixed-boundary corner.

Clearly, there is a pressing need to assess the degree of anisotropy in the mixed-boundary corner problem. From a fluid physics perspective, anisotropic effects due to the solid boundary will dominate over the effects of the free surface. However, the free surface acts to modify the wall-bounded turbulence and is not the principal source of anisotropy. Thus, unlike the problem studied by Walker *et al.* (1996), anisotropy in the mixed-boundary corner is highly three-dimensional. In the near-corner region, the effects of both the horizontal free surface and the vertical solid wall must be accounted for. (Of course, it would be expected that the results of Walker *et al.* 1996 would be applicable far from the wall.) The fundamental scientific issues in this study centre on understanding and modelling turbulent kinetic energy transport in the corner region where vertical no-slip boundary turbulence is influenced by the horizontal shear-free boundary.

1.2. *Problem statement*

The existence of mean secondary flows in the mixed-boundary corner adds a degree of complexity to the study of turbulence–free-surface interactions. Of particular interest

is the balance between kinetic energy production and dissipation in the near-corner region due to the combined effects of the free surface and no-slip boundaries. Terms in the energy balance equation have traditionally been extremely difficult to measure. However, with advanced optical diagnostics, such measurements are now feasible. Thus, the goal of this investigation was to employ high-resolution measurement systems to quantify and understand the mixed-boundary corner in terms of turbulent energy transport.

1.3. *A note on coordinates*

In this study, coordinates were chosen such that x, y, and z correspond to the stream, free-surface-normal, and wall-normal directions, respectively. The y- and z-coordinate directions are indicated in figure 1. Flow would be into the page for a right-hand coordinate system. The wall-normal coordinate, z, is zero at the wall and increases with distance from the wall. The free surface is located at $y = 0$ with gravity pointing in the negative y-direction. This coordinate system is consistent with that used in Grega *et al.* (1995), and was chosen such that motions toward the free surface are positive, $v > 0$, and depth below the free surface is negative.

2. Experimental apparatus and methods

2.1. *Flow facility*

Experiments were conducted in the large free-surface water tunnel facility at Rutgers University. The closed-circuit tunnel consisted of an upstream settling chamber, two-dimensional contraction, test section, downstream end tank, pumps, and piping. Details of the facility may be found in Smith (1992) and Grega *et al.* (1995).

The test section measured 58.4 cm in width $\times$ 122 cm in depth $\times$ 610 cm in length. It was constructed entirely from 1.91 cm thick glass panels placed in a welded steel I-beam frame. Flow was driven by two pumps operating in parallel. Variable speed controllers were used to set the flow rate between 760 l m^{-1} and 15 000 l m^{-1}. With the test section completely filled, the maximum flow rate corresponded to a mean free-stream velocity of approximately 30 cm s^{-1}. Free-stream turbulence levels were less than 0.1% of the mean free-stream velocity and the flow was uniform across the cross-section to within $\pm$2%.

2.2. *Video imaging and capture*

Video images for the digitized particle image velocimetry (DPIV) studies were made using a Texas Instruments TI-1134P high-resolution black-and-white multimode video camera. This camera had 1134 $\times$ 486 pixel resolution and could be configured to simultaneously image both even and odd video fields. For the final DPIV measurements, the camera was fitted with a 35 mm lens. Pairs of consecutive video frames comprising a DPIV video image pair were captured using an EPIX 4MIP-12 video capture board housed in a Pentium computer. The flow was illuminated using the beam from a Coherent Innova 70-5 5 W argon-ion laser which was swept into sheets of light using a galvanometer driven by a custom laser sweep circuit described in the following paragraph.

The functions of the laser sweep/timing circuit were to generate a galvanometer input signal and to serve as a trigger source for the video capture board. The galvanometer had a small front surface mirror mounted on its shaft; when the shaft rotated, a laser beam reflecting off the mirror swept out a sheet of light. The galvanometer input signal consisted of pairs of closely spaced voltage ramps. Each

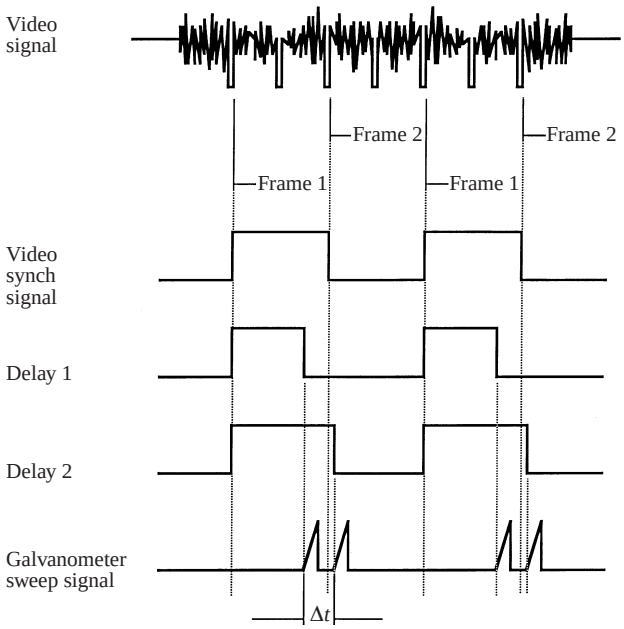

FIGURE 4. Representative timing diagrams for the video synchronization circuit. Observe that the galvanometer input signal consists of pairs of closely spaced voltage ramps which are synched to the video camera signal.

ramp caused the galvanometer shaft to rotate at a constant rotation speed to produce pairs of closely timed, short-duration, laser sheets, one at the end of one video frame (Frame 1) and a second at the beginning of the successive frame (Frame 2). These two frames would constitute a DPIV image pair. A timing diagram for this circuit appears in figure 4. Use of the sweep circuit made it possible to reduce the effective time between frames, Δt, to a few milliseconds even though the video system operated at 30 frames per second. One limitation of this technique, of course, was that one could only obtain image pairs at a rate of 15 Hz. The sweep signal was constantly monitored on a digital oscilloscope to ensure that the delay times, and consequently the Δt between sweeps, remained constant and synchronized with the video camera.

The same sweep circuit was also used as a trigger signal for the video capture system. While the sweep circuit generated a pair of triangular ramps for driving the galvanometer, the EPIX board was programmed to simultaneously capture the resulting video image pair and immediately write that pair from board memory to disk. The board was then instructed to wait 2 s while the sweep circuit continued to drive the galvanometer. After this delay, the signal triggering the next pair of laser sweeps would also be used by the EPIX board to capture that image pair. The process could continue indefinitely until all of the computer storage was filled. For these experiments 1000 image pairs were captured at even time intervals for each measurement location.

2.3. *DPIV processing program*

A DPIV software package was developed during this investigation; a detailed description of this program, its calibration, and accuracy is provided in Hsu (1999). A brief discussion of uncertainties is presented in the Appendix. The essence of the program is identical to that developed by Willert & Gharib (1991). That is, cross-correlations

of user-specified interrogation windows were computed in Fourier transform space to determine the mean displacement of particles contained in the windows. The principal feature of the current program was the two-step correlation process. First, a 'coarse' particle displacement field was generated using large overlapping† 128 pixel × 128 pixel interrogation windows to obtain a mean particle displacement for the centre of that window pair. The coarse displacement field was subsequently generated by moving the interrogation windows in quarter-window, i.e. 32 pixel, steps. This yielded an accurate, albeit highly spatially averaged, displacement field.

The displacement field generated by the coarse correlation stage was then used as a particle displacement estimator for the 'fine' correlation stage. In this stage, the interrogation windows could be made much smaller, as small as 16 pixels × 16 pixels. Instead of overlapping the fine correlation windows, however, the interrogation window in Frame 2 was displaced relative to its counterpart in Frame 1 by an amount determined by local interpolation of the coarse displacement field. In this manner, it was possible to accurately compute particle displacements larger than the fine interrogation window dimensions. Again the fine windows were incremented using quarter-window-sized steps. For the present data, the fine interrogation windows were 24 pixels × 48 pixels; given the pixel aspect ratio, this resulted in a roughly square window with edge dimensions corresponding to ~8.5 viscous lengths. The spacing between adjacent vectors corresponded to approximately 2.1 viscous lengths. The final steps in the DPIV routine were to convert pixel displacements to velocities and to apply a spatial Gaussian filter to the fine displacement field.

The end result was a processing program capable of generating extremely clean DPIV vector fields. As will be seen, this permitted accurate assessment of complex derivative quantities in the turbulent kinetic energy transport equation. The DPIV system was calibrated using a series of steps including translation and rotation of a pattern of dots as well as solid-body rotation of seeding particles in water. These tests are described in Hsu (1999).

2.4. *DPIV post processing*

The DPIV experiments consisted of positioning a horizontal laser sheet at different distances below the free surface and measuring streamwise and wall-normal velocity field data in those planes. At each location, 1000 individual image pairs were captured at 2 s intervals and processed using the cross-correlation routine outlined in the previous section.

After processing all of the image pairs at a given depth, the 1000 instantaneous vector fields were ensemble-averaged using a separate post-processing routine. Profiles of mean and fluctuating velocities as functions of distance from the wall were computed by averaging individual instantaneous vector fields along lines of constant distance from the wall, i.e. z = constant, and then ensemble averaging over the entire 1000 vector field data set. This was consistent with standard post-processing algorithms for computational data sets. In addition, local spatial derivatives were computed using central differences; averages of these derivatives were computed in the same manner as the mean and fluctuating velocities. Again, the reader is referred to the Appendix for a discussion of uncertainties. In addition, representative uncertainty limits are indicated on the data plots presented in § 3 and § 4 for Reynolds stress and higher-order quantities obtained from DPIV measurements. As discussed

† The interrogation window in Frame 2 had the same size and location as its counterpart in Frame 1.

in the Appendix, the uncertainty limits are based on the lower-bounds estimates of measurement resolution.

2.5. *LDV system*

Simultaneous streamwise and free-surface-normal velocity profiles in the wall-normal direction were made using a TSI Model 9100-10 five-beam, three-component LDV system.† Details of the LDV system and methodology appear in Grega (1995). The same argon-ion laser used for the DPIV system was also used by the LDV. Two blue beams, 488 nm, oriented in a vertical plane were used to measure the free-surface-normal velocity while three green beams, 514.5 nm, were aligned in a horizontal plane to provide streamwise and wall-normal velocity data. Frequency shifting, 40 MHz for the blue free-surface-normal signal and 40 MHz and 80 MHz for each of the two green signals, was used to resolve flow reversals and to improve temporal resolution.

To improve spatial resolution, the LDV optics package was augmented by placing a 500 mm focal length lens in the converging beam paths 22.2 cm from the standard 762 mm focal length beam converging lens. Beam convergence angles were thereby increased, resulting in smaller fringe spacings and smaller coincident measurement volumes. With the additional lens, the measurement volume was 1.1 mm long (in the wall-normal direction) and 0.04 mm in diameter. For comparison, the viscous length scale in the LDV studies was ~ 0.14 mm. Scattered light was collected in back-scatter mode. The system was calibrated using a small circular dish containing seeding particles in water moving in solid-body rotation. Details of the calibration may again be found in Grega (1995).

2.6. *LDV data acquisition and processing*

The key experimental performance criterion for the LDV measurements was acquisition of clean, temporally resolved, simultaneous velocities from the different LDV channels. For this reason, the burst and analogue signals from each channel were carefully monitored throughout the data acquisition process. Flow was seeded with 3 μm diameter TiO_2 particles in the crystalline rutile form. Aggressive use of thresholding and comparator accuracy coupled with judicious employment of electronic band-pass filtering ensured that extremely clean signals were obtained at sufficiently high data rates. Individual data rates for each LDV channel varied, from a minimum of 100 samples per s very close to the wall, to several hundred per s in the log region of the boundary layer. The analogue output from the three burst processors was simultaneously sampled at a rate of 50 samples per s using a LeCroy Model 8013A A/D converter. This comparatively low sampling rate ensured that the instantaneous signals from all three processors came from the same particle. In the context of flow time scales, the 20 ms sampling period corresponded to twice the viscous time scale of the boundary layer thereby ensuring that time-resolved velocity records were obtained. Because of the slowly evolving nature of the secondary flows, data records in excess of 40 min total duration were made at each measurement location. That is,

† In order to resolve the secondary flows, it was essential to accurately measure mean cross-stream velocities on the order of $1\,\mathrm{mm\,s^{-1}}$ within a turbulent field with fluctuations on the order of $10\,\mathrm{cm\,s^{-1}}$. The small beam convergence angles of most commercial systems, including the one used in this investigation, do not permit such measurements. The streamwise and free-surface-normal components can be measured directly with great accuracy. The wall-normal velocity, however, is a derivative quantity with much more limited accuracy. Consequently, only streamwise and free-surface-normal component data are included in this paper.

over 130K samples were taken for each velocity component, or LDV channel, at each measurement station.

Digitized signals were subsequently filtered using standard low-pass FFT filtering techniques to remove any remaining high-frequency noise. The cutoff filter frequency was chosen to correspond to ~ 10 viscous time scales based on the findings of Willmarth & Sharma (1984) that there are no turbulent fluctuations shorter than $10t^+$. Samples of raw and filtered signals along with complete LDV data sets are shown in Grega (1995). Finally, turbulence statistics were computed using simple ensemble averaging of the individual velocity measurements.

2.7. *Experimental methods*

The measurements reported in this paper were obtained over an extended period of time. The LDV experiments were done first followed some time later by the DPIV measurements. The combination of the two data sets was essential for cross-validation of the individual measurement techniques as well as for generating a more complete, three-dimensional data set. Cross-validation of the DPIV and LDV data was done in Hsu (1999). All measurements were made along the sidewall of the water tunnel 380 cm downstream of the test section inlet. A free-surface drain was installed in the downstream end tank to aid in maintaining a constant water level throughout the experiments. By continually adding water to the channel at a low fill rate and overflowing through the surface drain, a fixed water level could be maintained virtually indefinitely. In this manner, it was possible to measure velocity profiles at precisely determined distances below the free surface.

For both the LDV and DPIV experiments, measurements were made in planes parallel to the free surface. That is, for the LDV experiments, measurements of streamwise and free-surface-normal velocity were made as a function of horizontal distance from the tunnel sidewall. A series of seven profiles were obtained for different distances below the free surface, i.e. for $y^+ = -16$, -35, -57, -75, -120, and -190, and -4060. The last profile corresponded to the tunnel centre height where the boundary layer was nominally two-dimensional; it was used principally to determine the canonical boundary-layer friction velocity. In the DPIV studies, the laser sheet was aligned parallel to the free surface so that streamwise and wall-normal velocity field measurements were made. Again, the laser sheet position relative to the free surface was varied to obtain information as a function of depth below the surface. Seven DPIV experiments were conducted at different distances below the free surface, i.e. $y^+ = 0$, -19, -38, -57, -76, -95, and -133.

The LDV measurements were all made at a free-stream velocity of $20.6\,\mathrm{cm\,s^{-1}}$. The corresponding Reynolds number, Re_θ, was 1150. As noted previously, at each measurement location, over 130K simultaneous two-component velocity measurements were made at a 50 Hz sampling rate for a total sampling time in excess of 40 min.

DPIV measurements were made at a lower flow rate, nominally $12\,\mathrm{cm\,s^{-1}}$, corresponding to a Reynolds number, Re_θ, of 670. This was done primarily to improve spatial resolution. At this Reynolds number, with a camera field of view of ~ 3.3 cm in the stream direction, and ~ 2.5 cm in the wall-normal direction, the spacing between vectors in each DPIV velocity vector field was slightly larger than two viscous lengths. This was critical for calculating the instantaneous spatial derivatives found in the kinetic energy transport equation. In these experiments, 1000 DPIV image pairs were captured at 2 s intervals for total sampling times in excess of 30 min. As noted previously, such long times were again necessary to ensure resolution of the slowly evolving secondary flows.

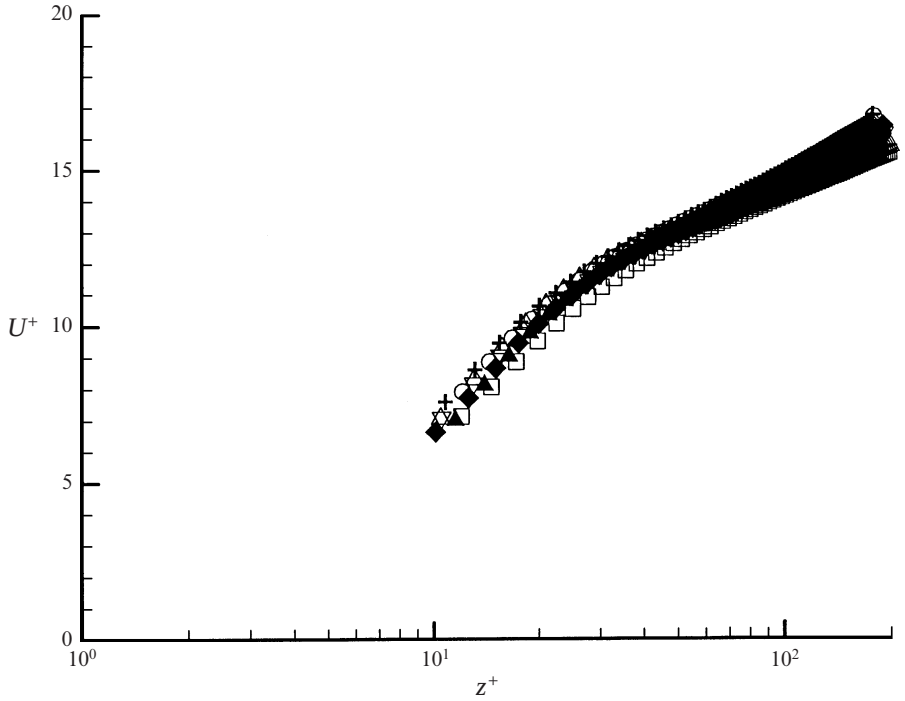

FIGURE 5. Mean streamwise velocity profiles, U^+ vs. z^+, obtained using DPIV for different distances from the free surface: □, $y^+ = 0$; △$y^+ = -19$; ▲, $y^+ = -38$; ▽, $y^+ = -57$; ◆, $y^+ = -76$; ○, $y^+ = -95$; +, $y^+ = -133$.

3. Results

This section contains a compilation of turbulence data obtained from the DPIV and LDV experiments. Complex derivative quantities in the turbulent kinetic energy transport equation, i.e. production, dissipation, diffusion, etc. are presented in § 4. It should be noted that all of the plots shown in the remainder of this paper have been non-dimensionalized by viscosity and the friction velocity corresponding to the 'deep'-water case. For the DPIV measurements, the friction velocity from the profile farthest from the free surface was used. As noted in Grega *et al.* (1995), the friction velocity decreases close to the free surface as a result of the free-surface current which thickens the boundary layer and reduces the wall shear. In order to isolate the effect of reduced wall shear close to the surface, a single reference friction velocity was used.

Figure 5 is a plot of mean streamwise velocity taken from the DPIV measurements at seven different distances below the free surface. Each individual mean velocity profile was fitted to the Clauser plot for a canonical turbulent boundary layer as a standard method of establishing the wall location and finding the friction velocity. When non-dimensionalized using a single reference u_τ value, as in figure 5, it can be seen that the non-dimensional mean velocity values at a fixed z^+ increase with increasing distance from the surface. This is merely an anomaly of the non-dimensionalization: since u_τ decreases close to the surface, dividing the actual mean velocity by a larger u_τ value simply reduces the dimensionless value.

A more interesting graph is the mean wall-normal velocity plot shown in figure 6. Data in this plot were again obtained from the DPIV experiments. Note that the maximum value on the ordinate is only $0.8u_\tau$; the mean velocity magnitudes are

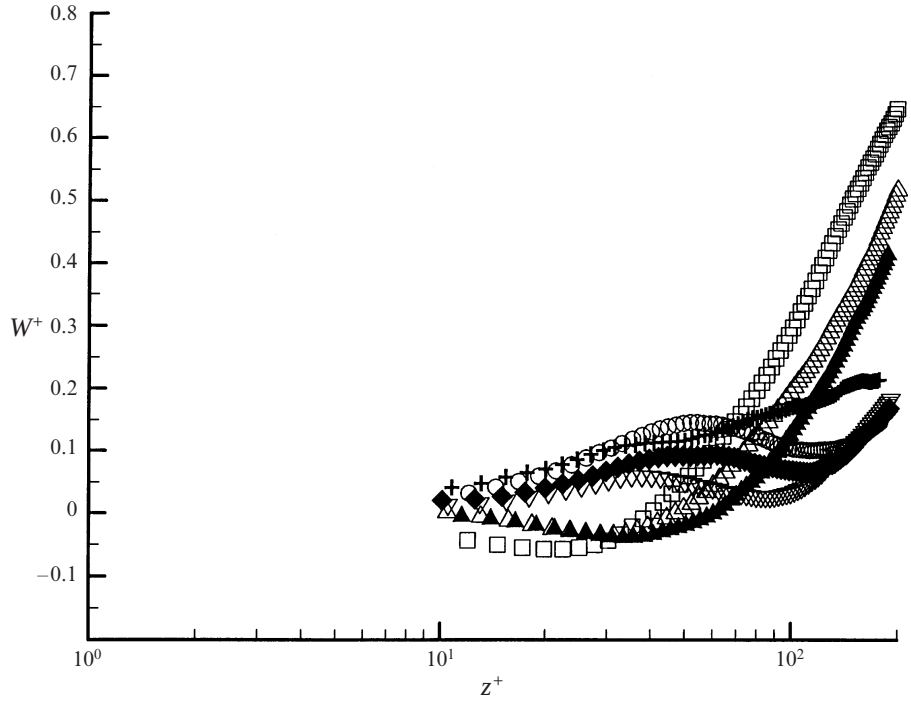

FIGURE 6. Mean wall-normal velocity profiles, W^+ vs. z^+, obtained using DPIV for different distances from the free surface. See caption of figure 5 for symbols.

less than $4\,\mathrm{mm\,s^{-1}}$. The key feature of figure 6 is the agreement between the mean wall-normal velocity profiles and what would be expected given the hypothesized secondary flow model shown in figure 1. For the three profiles closest to the free surface, W^+ values are slightly negative close to the wall, then become increasingly positive farther away. Based on the presumed existence of a secondary streamwise vortex in the near-corner region approximately 100 viscous lengths in diameter, one would anticipate that for $z^+ <\sim 50$, the inner secondary vortex would transport fluid inward toward the wall. Outside the inner secondary flow, lateral spreading of the outer secondary flow would appear as positive wall-normal velocities. This near-wall inflow combined with outflows farther from the wall may be seen in the near-surface data, for $y^+ = 0, -19$ and -38, shown in figure 6. The local maxima in W^+ for $y^+ = -57$, -76 and -95 are probably associated with the outflow of the inner secondary cell. The core of the cell appears to be located between $y^+ = -38$ and -57 as evidenced by the significant change in the velocity profile. Further away from the free surface, the inner secondary cell transports fluid in the positive z-direction, with the lower bound of the inner cell probably located between $y^+ = -95$ and -133, again as apparent in change in the velocity profile. The outer secondary cell is associated with the significant positive outflow near the free surface. Given that for $z^+ \gtrsim 100$, $\partial W/\partial z$ is much greater close to the free surface, for $0 < y^+ < -100$, than it is far from the surface, it is possible to conjecture that the outer secondary cell extends to a depth of approximately 100 viscous lengths beneath the interface.

Streamwise turbulence intensity profiles are shown in figure 7. Figure 7(*a*) includes data taken from the DPIV studies while the LDV measurements are shown in figure 7(*b*). Both data sets are included to provide a degree of independent validation of

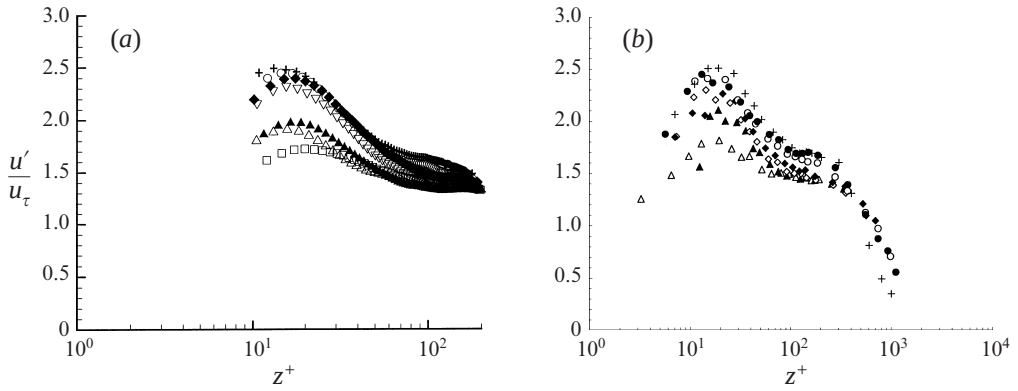

FIGURE 7. Streamwise turbulence intensity profiles, u'/u_τ vs. z^+, obtained (*a*) using DPIV and (*b*) using LDV for different distances from the free surface. See caption of figure 5 for symbols in (*a*). In (*b*): △, $y^+ = -16$; ▲, $y^+ = -35a$; ◇, $y^+ = -57$; ◆, $y^+ = -75$; ○, $y^+ = -120$; ●, $y^+ = -190$; +, $y^+ = -4060$.

the measurements. Note that there is strong quantitative agreement between the two data sets. Compare, for instance, individual profiles at $y^+ = -19$ and -76 in figure 7(*a*) with their counterparts, $y^+ = -16$ and -75, in figure 7(*b*).

The important feature of figure 7, however, is the decrease in steramwise fluctuations close to the free surface. Note that for depths greater than 100 viscous lengths from the free surface, the maximum non-dimensional streamwise intensity value is ~ 2.5 and may be found around $z^+ = 20$. At the free surface, however, the maximum value of u'/u_τ is only 1.7, a reduction of over 30%.

It is worth noting that for $z^+ \gtrsim 30$, u'/u_τ values at the free surface become larger than the corresponding u'/u_τ measurements in the next two lower profiles taken at $y^+ = -19$ and -38. This means that farther from the wall, the streamwise fluctuations actually begin to increase again in the 10 to 20 viscous lengths closest to the surface. This is consistent with the computational findings reported by Walker *et al.* (1996) for isotropic turbulence in the vicinity of a free surface. The difference between the present work and that of Walker *et al.* (1996) is that the rebound in u'/u_τ is not uniform across the surface. In the viscous sublayer and buffer regions, u'/u_τ continues to decrease all the way to the surface.

Reduction in free-surface-normal fluctuations, v'/u_τ, across the entire free surface can be seen in the LDV data shown in figure 8. This result is necessitated by the zero vertical velocity condition at the free surface for this very low-Froude-number flow. Like the u'/u_τ data, one can see that the data approach the canonical boundary layer profile at depths greater than 200 viscous lengths below the free surface.

Wall-normal turbulence intensities taken from the DPIV studies are plotted in figure 9. A general decrease in w'/u_τ approaching the free surface is easily observed. This is similar to the trends observed for the fluctuations of the other two components. In addition, like the u'/u_τ profiles, values of w'/u_τ at the free surface becomes larger than corresponding values in the next two lower profiles (i.e. at $y^+ = -19$ and -38) for $z^+ \gtrsim 40$. In fact, for $z^+ \gtrsim 100$, values of w'/u_τ at the free surface are larger than their counterparts as far below the surface at $y^+ = -95$. Thus, for the log region and further away from the wall, results similar to those reported by Walker *et al.* (1996) are observed. That is, the surface-parallel fluctuations decrease to a minimum a small distance below the free surface, in this case within 20 viscous lengths of

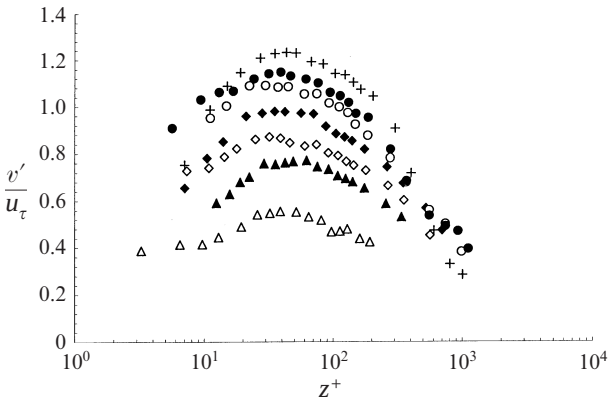

FIGURE 8. Free-surface-normal turbulence intensity profiles. v'/u_τ vs. z^+, obtained using LDV for different distances from the free surface. See caption of figure 7(*b*) for symbols.

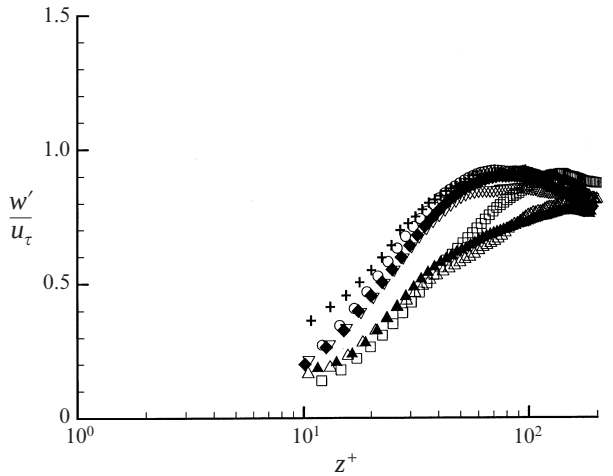

FIGURE 9. Wall-normal turbulence intensity profiles, w'/u_τ vs. z^+, obtained using DPIV for different distances from the free surface. See caption of figure 5 for symbols.

the surface, and begin to rebound in the thin layer immediately adjacent to the free surface. Free-surface-normal fluctuations necessarily approach zero at the surface for the zero-Froude-number case.

The presence of the solid wall, however, causes a different effect in the near-wall region. In the viscous sublayer and the inner part of the buffer region, all three components of turbulence intensity monotonically decrease all the way to the free surface. This is probably an effect of the inward and downward motion of the inner secondary vortex in the very near-corner region. The division between the inner secondary vortex and the outer secondary flow therefore also appears to separate near-surface regions where surface-parallel energy rebounds close to the surface (i.e. for $z^+ \gtrsim 50$) and where surface-parallel fluctuations decrease continuously up to the free surface.

The effect of the free surface and the demarcation between inner and outer secondary flow regions are also evident in the Reynolds stress data, $-\langle uw \rangle / u_\tau^2$ and

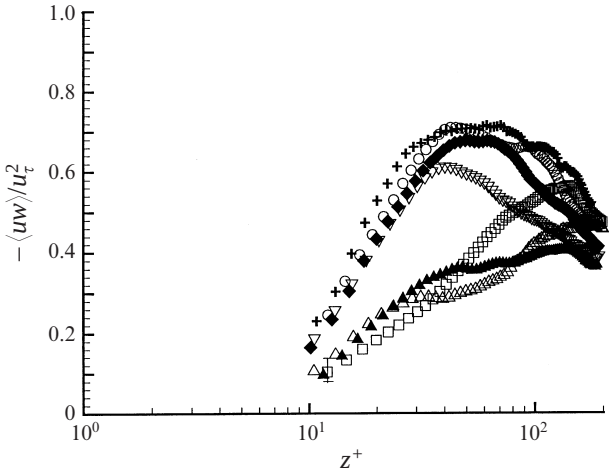

FIGURE 10. Reynolds stress profiles, $-\langle uw\rangle/u_\tau^2$ vs. z^+, obtained using DPIV for different distances from the free surface. See caption of figure 5 for symbols. Lower-bound uncertainty estimates are indicated by a representative error bar.

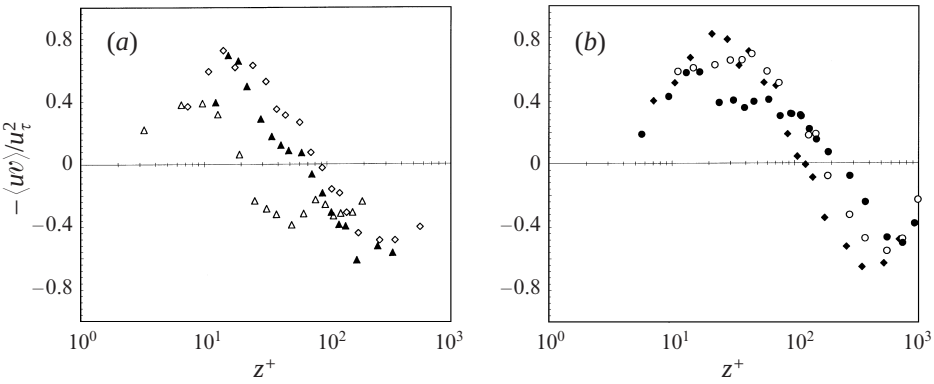

FIGURE 11. Reynolds stress profiles, $-\langle uv\rangle/u_\tau^2$ vs. z^+, obtained using LDV: (*a*) for locations closest to the free surface, and (*b*) for locations farthest from the free surface. See caption of figure 7(*b*) for symbols.

$-\langle uv\rangle/u_\tau^2$, shown plotted versus z^+ in figures 10 and 11, respectively. In figure 10, the $-\langle uw\rangle/u_\tau^2$ profiles taken at $y^+ = -57$ and below are qualitatively and quantitatively consistent with canonical turbulent-boundary-layer Reynolds stress profiles at this Reynolds number. Like the turbulence intensity data, the maximum value of each profile decreases as the free surface is approached. The three profiles closest to the free surface are, however, markedly different. Not only are the magnitudes of the profile maxima less than the maximum in a canonical boundary layer, but the locations of the maxima are much further from the wall in the three free-surface profiles. This is believed to be a result of the thickening of the boundary layer at the free surface.

Careful examination of the three $-\langle uw\rangle/u_\tau^2$ profiles closest to the free surface again indicate a crossing of the free-surface profile over the next two lower profiles around $z^+ = 30$ to 40. Like the streamwise and wall-normal turbulence intensity profiles, the Reynolds stress values at the free surface close to the wall are less than the corresponding values in the two profiles at $y^+ = -19$ and $y^+ = -38$. For $z^+ > 60$,

the values of $-\langle uw\rangle/u_\tau^2$ at the free surface become significantly larger than the values in the next two profiles: there is a dramatic rebound in $-\langle uw\rangle/u_\tau$ very close to the free surface. It is also interesting to note that the $y^+ = -19$ profile crosses over the $y^+ = -38$ profile around $z^+ = 80$. The change in the location of the maxima of $-\langle uw\rangle/u_\tau^2$ may also be due to advective effects.

The correlation between the streamwise and free-surface-normal fluctuations, $-\langle uv\rangle/u_\tau^2$, show equally significant variations with distance below the free surface. For clarity, three profiles closest to the surface, roughly corresponding to the upper half of the inner secondary cell, are shown in figure 11(*a*) while three profiles farther from the surface are shown in figure 11(*b*). At the channel centre height, $-\langle uv\rangle/u_\tau^2$ approaches zero everywhere. Observe that for all profiles appearing in figure 11, $-\langle uv\rangle/u_\tau^2$ is positive close to the wall and negative farther away. Negative values of $-\langle uv\rangle/u_\tau^2$ indicate that an upward, $v > 0$, motion carries with it higher, $u > 0$, streamwise momentum. One would expect to see negative Reynolds stresses in the outer region of the boundary layer close to the free surface. Due to the thickening of the boundary layer at the free surface, positive vertical motions transport higher-momentum free-stream fluid upwards into the thicker lower-momentum turbulent boundary layer at the free surface.

Positive $-\langle uv\rangle/u_\tau^2$ values close to the wall are more difficult to explain. It would probably not be correct to simply associate these trends with the inward and downward motion of the inner secondary vortex close to the free surface. The principal reason for this is that positive $-\langle uv\rangle/u_\tau^2$ values are found below the hypothesized extent of the inner secondary vortex, i.e. $y^+ < -120$. The actual size and strength of the secondary flows are the topic of an ongoing investigation.

4. Discussion

In the preceding section, detailed DPIV and LDV measurements made in the near-corner region were presented. These data support the conclusion of Grega *et al.* (1995) that secondary flows generated by flow along a vertical solid wall close to a horizontal free surface include an inner secondary vortex and an outer secondary flow. There also appears to be at least qualitative agreement of the mean flow features with the LES calculations of Thomas & Williams (1995) and to a lesser degree with Sreedhar & Stern (1998). As indicated in figure 3, however, the details of the turbulence are an open issue. The purpose of this discussion is to examine the kinetic energy transport in the near-corner region. Data presented in the preceding section will be used to assess the degree of anisotropy of the energy transport and to gain insight into the nature of the energy balance in that region. Conducting this exercise will provide guidance and quantitative metrics for subsequent anisotropic turbulence model development.

A key advantage of the present measurements is that they permit such a highly detailed analysis of the flow. For instance, it was shown in § 3 that all three components of turbulence intensity along with $-\langle uw\rangle$ Reynolds stress decrease significantly approaching the free surface. While the free-surface-normal motions, v', necessarily continue to decrease to a minimum at the free surface, since for the zero-Froude-number limit free-surface-normal motions must become zero at $y = 0$, the free-surface-parallel statistics, u', w', and $-\langle uw\rangle$, generally begin to increase again in a very thin layer immediately adjacent to the free surface. The exception to this trend occurs at the free surface close to the wall in the vicinity of the inner secondary vortex. In this region, free-surface-parallel motions continue to decrease all the way to the free surface. The focus of this discussion, then, is to examine these trends in the context of turbulent

kinetic energy transport. This analysis will also provide insight into the problem of modelling turbulence in the mixed-boundary corner.

The mean turbulent kinetic energy transport equation is obtained by taking the dot product of velocity with the instantaneous momentum equations, performing a Reynolds decomposition, and averaging. The resulting equation takes the following form:

$$\underset{\text{advection}}{(\mathrm{D}/\mathrm{D}t)\{\langle u_i^2\rangle/2\}} = \underset{\text{production}}{-\langle u_i u_j\rangle \partial U_i/\partial x_j} + \underset{\text{pressure transport}}{-(1/\rho)(\partial/\partial x_i)\{\langle p u_i\rangle\}} + \underset{\text{turbulent transport}}{-(\partial/\partial x_j)\{\langle u_j u_i^2\rangle/2\}} + \underset{\text{diffusion}}{2\nu(\partial/\partial x_j)\{\langle u_i S_{ij}\rangle\}} - \underset{\text{dissipation}}{2\nu\langle S_{ij}^2\rangle}, \quad (1)$$

where $S_{ij} = \frac{1}{2}\{\partial u_i/\partial x_j + \partial u_j/\partial x_i\}$ is the rate-of-strain tensor. The identification label beneath each term in the equation provides a brief physical interpretation for that term. Recall that only the production and dissipation terms can cause net changes in the total energy in the flow. The production term describes the generation of turbulent kinetic energy through interaction with mean velocity gradients. Dissipation represents the loss of mechanical energy through conversion to thermal energy. The remaining terms on the right-hand side of (1) account for the transfer of energy within the flow and between scales.

Before proceeding, it is important to recognize that it is not possible to completely measure any term in (1) using only DPIV measurements from horizontal laser sheets. (It is, of course, not possible to directly measure the pressure transport term at all.) Each of the remaining terms in the turbulent kinetic energy equation contains three-dimensional spatial derivatives of all three component velocities. It is in principle necessary to make DPIV measurements in all three component planes.

The presence of the rigid wall in this flow, however, means that gradients in the wall-normal direction, specifically mean and fluctuating gradients of streamwise velocity, $\partial U/\partial z$ and $\partial u/\partial z$, will dominate virtually every term in (1). This will be true particularly in the near-wall region. It is therefore argued that reasonably accurate estimates of all but the pressure transport term can be made using (x, z) velocity field data. Additional measurements of turbulence production and dissipation in the (y, z) plane are included in Hsu (1999). These terms show a negligible contribution to the energy budget in the near-corner region and thereby confirm the dominance of the streamwise velocity gradients in the wall-normal direction. Nonetheless, the reader should keep in mind that the energy transport equation data shown include only those components which could be calculated from velocity field measurements in free-surface-parallel planes and there is a concomitant loss of accuracy from omitting out-of-plane derivative quantities.

With this in mind, figure 12(*a*) shows turbulence kinetic energy production as a function of distance from the wall for eight different distances from the free surface. For reference, an error bar has been placed on the measurement closest to the free surface and wall. The magnitude of the error bar corresponds to the lower-bound uncertainly estimate computed in the Appendix. Similar uncertainty limits are indicated for each of the plots comprising figure 12.

Observe that the production profile in figure 12(*a*) obtained at $y^+ = -133$ has a maximum value of 0.16. This peak value is located approximately 15 viscous lengths from the wall which is consistent with production profiles for canonical turbulent boundary layers. The salient feature of the plot, then, is the fact that production decreases dramatically approaching the free surface. The maximum dimensionless production value at the free surface is ~ 0.04. This represents a 75% decrease from

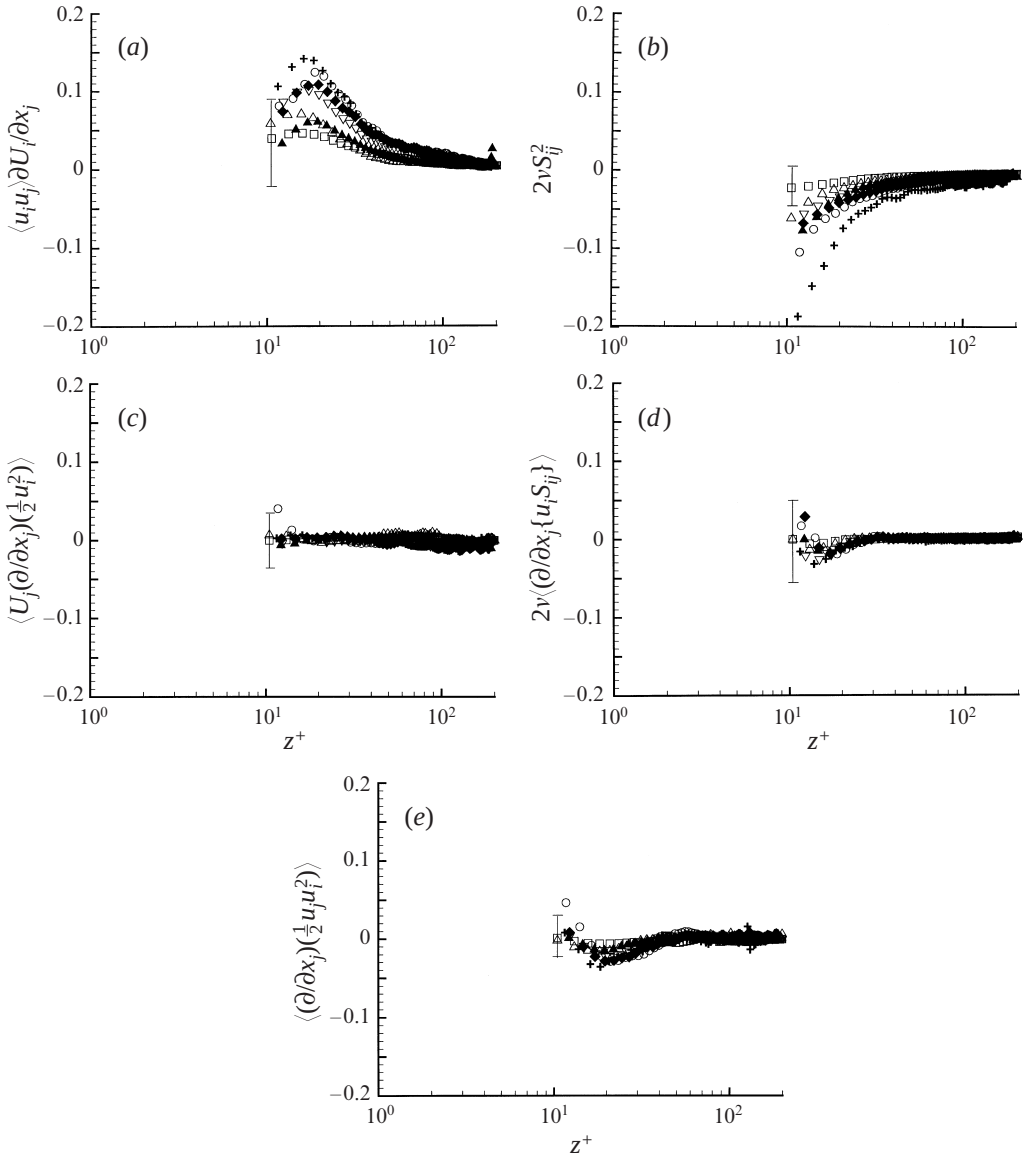

FIGURE 12. Wall-normal profiles showing contributions from the (x, z)-plane for different distances below the free surface for the following: (*a*) turbulent kinetic energy production, $-\langle u_i u_j \rangle \partial U_j / \partial x_j$; (*b*) turbulent dissipation, $-2\nu \langle S_{ij}^2 \rangle$ (where $S_{ij} = 1/2\{\partial u_i/\partial x_j + \partial u_j/\partial x_j\}$); (*c*) turbulent kinetic energy advection, $\langle U_j (\partial/\partial x_j)\{u_i^2/2\} \rangle$; (*d*) viscous diffusion, $2\nu \langle (\partial/\partial x_j)\{u_j S_{ij}\} \rangle$; (*e*) turbulent kinetic energy transport, $\langle (\partial/\partial x)\{u_j u_i^2/2\} \rangle$. See the caption of figure 5 for symbols. In all plots, lower-bound uncertainly estimates are indicated by a representative error bar.

the canonical boundary layer value. It is believed that this decrease in production approaching the free surface is the reason why the free-surface-parallel components of turbulence intensity also decrease within 100 viscous lengths of the free surface. The slight recovery in the 20 viscous lengths closest to the surface is discussed later in this section. Attenuation of vertical motions is, of course, necessitated by the no-through-flow boundary condition at the free surface.

The dramatic decrease in production could have been anticipated after further examining the mean streamwise velocity profiles, figure 5, and the $-\langle uw \rangle$ Reynolds stress data in figure 10. One can see that the non-dimensional mean velocity profile is not significantly altered by the free surface. However, while the $-\langle uw \rangle$ Reynolds stress profiles farther from the free surface reach a maximum around $z^+ = 40$, the free-surface profile peaks beyond $z^+ = 100$. Thus, at the free surface, the Reynolds stress values are small where the mean shear is large and vice versa; production is sharply diminished.

Figure 12(*b*) shows that the reduced production approaching the free surface is accompanied by a reduction in dissipation as well. In this plot, wall-normal profiles of dissipation are shown for various depths below the free surface. (The reader is reminded that only components of dissipation which could be computed from the DPIV data are included in the dissipation sums.) Like production, dissipation decreases dramatically with decreasing distance from the free surface. As seen in figure 12(*b*), there is a 90% reduction in the maximum calculated dissipation values between the $y^+ = -133$ profile and the free-surface profile. Again, a representative error bar is included in the figure to indicate the lower bound estimate of uncertainty for these measurements.

Decreases in turbulent kinetic energy dissipation at a free surface were extensively examined by Walker *et al.* (1996). In their study the turbulence was initially isotropic before being subjected to the free-surface boundary condition and there were no additional boundary conditions imposed at the edges of their computational domain. With this simpler flow, they demonstrated that the increase in surface-parallel turbulence intensities was a direct result of reduced dissipation at the free surface.

In the present study, the reduction in dissipation is also accompanied by an increase in surface-parallel turbulent fluctuations at the free surface. This was observed in the 20 viscous lengths closest to the free surface. A key difference between the present turbulence intensity data for the mixed-boundary corner and data from the isotropic turbulence study of Walker *et al.* (1996) is the observed decrease in u' and w' in the range $-100 < y^+ < -20$ before the increase in the final 20 viscous lengths; isotropic turbulence at a free surface does not exhibit the region of reduced surface-parallel intensities. The recovery in surface-parallel fluctuating velocities was noted farther from the wall, for $z^+ > 50$, in regions associated with the outer secondary flow. Close to the wall, however, all three components of turbulence intensity approach a minimum at the free surface. This is all part of the complexity resulting from the close proximity of the shear-free free surface and the orthogonal no-slip wall.

In a canonical turbulent boundary layer, the kinetic energy redistribution is necessitated by the misalignment of the production and dissipation peaks. Dissipation is a maximum at the wall, where velocity gradients are largest, while the production peak is located approximately 15 viscous lengths away from the wall. The redistribution terms, pressure transport, turbulent transport, and viscous diffusion, act to transport energy throughout the flow such that the substantial derivative of kinetic energy, the advection term, remains zero everywhere.

The presence of the free surface creates a situation where kinetic energy may be transported in both the free-surface-normal, i.e. spanwise, as well as wall-normal directions. Thus, it would be instructive to acquire information about the other terms in (1) for different distances below the free surface. Plots of advection, diffusion, and turbulent transport profiles for different y^+ locations are shown in figures 12(*c*), 12(*d*), and 12(*e*), respectively. Again, note that only contributions from the (x, z)-plane could be included in the calculations. The advection profiles, computed using

the substantial derivative, are included as an internal check on the energy transport calculations.

Wall-normal profiles of viscous diffusion are presented in figure 12(*d*). Observe that this term is essentially zero everywhere except near the wall, $z^+ \leqslant 30$. Around $z^+ = 15$, the diffusion term at all depths is slightly negative, between -0.04 far from the free surface and -0.01 at the surface. The location of these minima coincides with the location of the production peaks. Viscous diffusion acts to transport part of the turbulent energy which is generated by interactions with the mean flow and is not converted to heat through dissipation.

Taken *in toto*, the energy balance in the mixed boundary corner appears to be highly complex. The free surface plays an important role in the rate of kinetic energy production and dissipation. But the solid vertical wall significantly affects the energy transport as well. If for no other reason, it is the ultimate source of the turbulence. As a result, the energy balance changes as functions of distance from the wall and distance from the free surface. This strong spatial variation in how energy is produced, redistributed, and dissipated makes the turbulence-modelling problem difficult indeed while providing a wealth of interesting phenomena to be examined.

5. Conclusions

Detailed DPIV and LDV measurements were made to examine the energy transport in a turbulent boundary layer formed by flow along a vertical wall with a horizontal free surface. Wall-normal profiles of turbulent boundary layer statistics and energy transport equation terms were acquired for different distances below the free surface. Careful examination of the data led to the following conclusions:

(i) between 20 and 100 viscous lengths of the free surface, for all z^+, reductions in turbulence production results in a decrease in surface-parallel turbulence intensities;

(ii) within 20 viscous lengths of the free surface, for $z^+ > 50$, reductions in turbulence dissipation results in an increase in surface-parallel turbulence intensities;

(iii) within 20 viscous lengths of the free surface, but for $z^+ < 50$, all three components of turbulent motions decrease to a minimum at the free surface;

(iv) the decrease in (iii) is because the near-corner energy balance is significantly different than elsewhere in the flow; the magnitudes of all terms on the right-hand side of the turbulent kinetic energy equation, although small, appear to be of equal order.

Partial support for this research from the Office of Naval Research (Grant# N00014-92-J-1020) through Dr Edwin P. Rood is gratefully acknowledged.

Appendix. DPIV measurement uncertainties

The principal goal in developing a DPIV processing program was to be able to generate accurate, high-resolution vector fields for computing complex turbulence transport quantities. To this end, the DPIV system was calibrated using a series of steps including translation and rotation of a pattern of dots as well as solid-body rotation of seeding particles in water. These tests are described in Hsu (1999). Benchmarking of this capability on a canonical flat-plate turbulent boundary layer also appears in Hsu (1999) and will be published in a separate article. In that study, turbulent kinetic energy production, dissipation, and diffusion profiles were obtained

which matched DNS calculations. This Appendix contains a brief uncertainty analysis for the current Δ-wing vortex measurements.

It is important to note at the outset that there are two classes of uncertainty which must be accounted for. The first uncertainty, ε, is associated with convergence of averages for finite sample sizes. For this class of uncertainties, Lumley & Panofsky (1964) provide the following equation for calculating uncertainties:

$$\varepsilon/U_\infty = \{\, 2\, I(u'/U_{local})^2/T \}^{1/2} \tag{A 1}$$

where I is the integral time scale of the flow, and T represents the total sampling time. In this case, the integral time scale can be estimated as δ/U_∞ where δ is the boundary layer thickness. For this flow, the boundary layer thickness is approximately 5.7 cm for a free-stream velocity of 12 cm s^{-1}. In this case, then, the integral time scale is approximately 0.48 s. The sampling period is 2000 s, and u'/U_{local} is estimated to be 0.3. Substitution into (A 1) yields a value for ε of 0.0065 cm s^{-1} or $\varepsilon^+ = 0.010$.

The second uncertainty, e, arises from the accuracy and resolution of the DPIV measurement technique. It should be pointed out at the outset that there is a range of uncertainty estimates in the literature for particle displacement measurements ranging from $O(0.01)$ pixels by Raffel, Willert & Kompenhans (1998) at the low end to the more commonly accepted $O(0.1)$ pixel uncertainty put forward by Keane & Adrian (1992, 1993), their typical uncertainty is ~ 0.05 pixels. It is the authors' opinion, based on actual scatter in the data and the reproducibility of the measurements, that the actual uncertainty for the present measurements is much closer to the lower than the upper bound. For the purposes of this discussion, however, the values presented by Raffel *et al.* (1998) and Keane & Adrian (1992), respectively, serve as upper and lower bounds for the measurement uncertainty. It should also be noted here that R. J. Adrian (1998, personal communication) emphasized that the use of fractional pixel displacement as an uncertainty metric contains an implicit assumption that the mean particle image size is 2–3 pixels which was, in fact, the case for the present measurements.

In their monograph, Raffel *et al.* (1998) identified a number of sources of uncertainty for PIV and DPIV measurement systems. The three relevant uncertainties for this experiment are particle image size in pixels, particle displacement in pixels, and particle image density. Based on the analysis of Raffel *et al.* (1998) and examination of the video images captured in this study, the uncertainties for each of these sources are on the order of 0.01 pixels; the corresponding velocity uncertainty is 0.0058 cm s^{-1}. From the work of Kline & McClintock (1953) the combined measurement uncertainty for all three sources of uncertainty is simply the square root of the sum of the squared uncertainties; i.e. $e \approx 0.010$ cm s^{-1}, or $e^+ = 0.016$.

As noted earlier, the analysis of Raffel *et al.* (1998) should really be viewed as an idealized estimate. A more commonly accepted estimate, developed by Keane & Adrian (1992) among others, is 0.05 pixels. This translates to 0.029 cm s^{-1} for the uncertainty of an instantaneous velocity measurement. Uncertainties of derivative turbulence quantities were then calculated using both the Raffel *et al.* (1998) and Keane & Adrian (1992) analyses and are presented here as upper and lower bounds for the present measurements.

To calculate uncertainties in measured and derived quantities, then, a few simple rules were used. First, uncertainties for quantities involving mean velocities were assumed to be functions of ε, while uncertainties of fluctuating velocities were calculated as functions of e. Second, products or quotients of quantities were assumed to have uncertainties equal to the sum of the component uncertainties. Third, uncertainties

Quantity	Formula	Uncertainty range (non-dimensional)
Mean velocities: U_i	ε	0.010
Turbulence intensities: u_i'	e	0.016–0.080
Reynolds stresses: $-\langle u_i u_j \rangle$	$2e$	0.031–0.16
TKE advection: $U_j(\partial/\partial x_j)\{\langle u_i^2 \rangle/2\}$	$\sqrt{2}\{\varepsilon + 2e/\Delta x\}$	0.035–0.18
TKE production: $-\langle u_i u_j \rangle \partial U_i/\partial x_j$	$\sqrt{3}\{2e + \sqrt{2}\varepsilon/2(\Delta x)\}$	0.060–0.30
TKE transport: $(-\partial/\partial x_j)\{\langle u_j u_i^2 \rangle/2\}$	$(1 + 2\sqrt{2})e/\Delta x$	0.027–0.14
TKE diffusion: $2\nu(\partial/\partial x_j)\{\langle u_i S_{ij} \rangle\}$	$\sqrt{6}e\{1 + 1/\Delta x\}$	0.056–0.28
TKE Dissipation: $\langle\{\partial u_i/\partial x_j + \partial u_j/\partial x_i\}^2\rangle$	$2\sqrt{3}e/\Delta x$	0.025–0.13

TABLE 1. Non-dimensional uncertainties for all the plots in the paper.

of sums or differences were equal to the square root of the sum of the squared component uncertainties. Finally, uncertainties associated with derivatives were computed by multiplying the uncertainty of the dependent variable by $\sqrt{2}$ and dividing by the differential length. For central differences, the differential length was twice the vector spacing.

Using these rules, non-dimensional uncertainties were computed for all of the plots presented in the body of this paper. These are shown in table 1, including the formulae derived for each quantity. For uncertainties which are functions of e, upper and lower bounds are provided. Non-dimensionalization was done in the same manner as the corresponding plot. In general, it can be seen that the degree of scatter in the data falls well within the bounds of the limits defined through the works of Raffel *et al.* (1998) and Keane & Adrian (1992). Based on the scatter in the present data, it appears that the velocity measurement uncertainty is much closer to the lower 0.01 pixel bound than the upper 0.1 pixel bound. A representative error bar has been included in each of figures 10 and 12 showing the lower bound estimate of uncertainty for the corresponding quantities. Note that the uncertainties for mean and fluctuating velocities were smaller than the plotter symbols.

REFERENCES

ANTHONY, D. G. & WILLMARTH, W. W. 1992 Turbulence measurement in a round jet beneath a free surface. *J. Fluid Mech.* **243**, 699.

GESSNER, F. B. & JONES, J. B. 1961 A preliminary study of turbulence characteristics of flow along a corner. *Trans. ASME* D: *J. Basic Engng* **83**, 657.

GESSNER, F. B. & JONES, J. B. 1965 On some aspects of fully-developed turbulent flow in rectangular channels. *J. Fluid Mech.* **23**, 689.

GREGA, L. M. 1995 Generation of secondary flows in turbulent flow along a solid wall-free surface corner. PhD dissertation, Rutgers University.

GREGA, L. M., WEI, T., LEIGHTON, R. I. & NEVES, J. C. 1995 Turbulent mixed-boundary flow in a corner formed by a solid wall and a free surface. *J. Fluid Mech.* **294**, 17.

HSU, T. Y. 1999 Turbulent transport in the mixed boundary corner formed by flow along a solid wall close to a free surface. MS thesis, Rutgers University.

HUNT, J. C. R. & GRAHAM, J. M. R. 1978 Free-stream turbulence near plane boundaries. *J. Fluid Mech.* **84**, 209.

KEANE, R. D. & ADRIAN, R. J. 1992 Theory of cross-correlation analysis of PTV images. *Appl. Sci. Res.* **49**, 191.

KEANE, R. D. & ADRIAN, R. J. 1993 Prospects for super-resolution with particle image velocimetry. *Proc. SPIE; Optical Diagnostics in Fluid and Thermal Flow* **2005**, 283.

Kline, S. J. & McClintock, F. A. 1953 Describing uncertainties in single-sample measurements. *Mech. Engng* **75**, 3.

Logory, L. M., Hirsa, A. & Anthony, D. G. 1996 Interaction of wake turbulence with a free surface. *Phys. Fluids* **8**, 805.

Longo, J., Huang, H. P. & Stern, F. 1998 Solid/free-surface juncture boundary layer and wake. *Exps. Fluids* **25**, 283.

Lumley, J. L. & Panofsky, H. A. 1964 *The Structure of Atmospheric Turbulence*. Interscience.

Perot, J. P. & Moin, P. 1995 Shear-free turbulent boundary layers. Part 1. Physical insights into near-wall turbulence. *J. Fluid Mech.* **295**, 199.

Raffel, M., Willert, C. E. & Kompenhans, J. 1998 *Particle Image Velocimetry*, Springer.

Shah, P. N., Atsavapranee, P., Hsu, T. Y., Wei, T. & McHugh, J. 2000 Role of turbulent elongational stresses on deflocculation in paper sheet formation. *TAPPI J.* **83**.

Smith, G. B. 1992 Turbulent cascade in colliding off-axis vortex rings. MS thesis, Rutgers University.

Sreedhar, M. & Stern, F. 1998 Large eddy simulation of temporally developing juncture flows. *Intl J. Numer. Meth. Fluids* **28**, 47.

Thomas, N. H. & Hancock, P. E. 1977 Grid turbulence near a moving wall. *J. Fluid Mech.* **82**, 481.

Thomas, T. G. & Williams, J. J. R. 1995 Large eddy simulation of turbulent flow in an asymmetric compound open channel. *J. Hydraul. Res.* **33**, 27.

Uzkan, T. & Reynolds, W. C. 1967 A shear-free turbulent boundary layer. *J. Fluid Mech.* **28**, 803.

Walker, D. T., Leighton, R. I. & Garza-Rios, L. O. 1996 Shear-free turbulence near a flat free surface. *J. Fluid Mech.* **320**, 19.

Willert, C. & Gharib, M. 1991 Digital particle image velocimetry. *Exps. Fluids* **10**, 181–193.

Willmarth, W. W. & Sharma, L. 1984 Study of turbulent structure with hot wires smaller than the viscous length. *J. Fluid Mech.* **142**, 121.